Article

Propane Dehydrogenation over Cobalt Aluminates: Evaluation of Potential Catalytic Active Sites

Aleksey N. Chernov, Svetlana V. Cherepanova [ID], Evgeny Yu. Gerasimov [ID], Igor P. Prosvirin [ID], Galina A. Zenkovets, Alexei A. Shutilov, Anna S. Gorbunova, Konstantin Yu. Koltunov *[ID] and Vladimir I. Sobolev *

Boreskov Institute of Catalysis, Russian Academy of Sciences, Pr. Akademika Lavrentieva, 5, Novosibirsk 630090, Russia; anch@catalysis.ru (A.N.C.); svch@catalysis.ru (S.V.C.); gerasimov@catalysis.ru (E.Y.G.); prosvirin@catalysis.ru (I.P.P.); zenk@catalysis.ru (G.A.Z.); alshut@catalysis.ru (A.A.S.); gorbunova@catalysis.ru (A.S.G.)
* Correspondence: koltunov@catalysis.ru (K.Y.K.); visobo@catalysis.ru (V.I.S.)

Abstract: Non-oxidative propane dehydrogenation (PDH) is becoming an increasingly important approach to propylene production, while cobalt-containing catalysts have recently demonstrated great potential for use in this reaction, providing efficiencies comparable to those of industrially employed Pt- and Cr-based catalytic systems. It is therefore essential to clarify the nature of their active sites, especially since contradictory opinions on this issue are expressed in the literature. In this study, efforts were made to determine the state of Co in cobalt aluminates ($CoAl_2O_4$-Al_2O_3) responsible for PDH under typical operating conditions (600 °C, 1 atm). It is shown that the catalyst with a low cobalt content (Co/Al = 0.1) ensured the highest selectivity to propylene, ca. 95%, while maintaining significant propylene conversion. The structural motifs such as cobalt oxide and metallic cobalt nanoparticles, in addition to tetrahedral Co^{2+} species in the $CoAl_2O_4$ spinel system, were evaluated as potential active-site ensembles based on the obtained catalytic performance data in combination with the XRD, H_2-TPR, TEM and XPS characteristics of as-synthesized, spent and spent–regenerated catalysts. It is revealed that the most likely catalytic sites linked to PDH are the Co-oxide forms tightly covering alumina or embedded in the spinel structure. However, additional in situ tuning is certainly needed, probably through the formation of surface oxygen vacancies rather than through a deeper reduction in Co^0 as previously thought.

Keywords: propylene; propane dehydrogenation; cobalt catalysts; heterogeneous catalysis; reaction mechanism

1. Introduction

Propylene, one of the basic organic chemicals, is largely produced by non-selective and energy-intensive naphtha steam cracking and fluid catalytic processes [1]. However, given the increased availability of propane as a feedstock, non-oxidative propane dehydrogenation (PDH) is now growing in importance as the most targeted and atom-efficient propylene production route [1–10]. Nonetheless, it is noteworthy that Pt- and CrO_x-based catalysts commonly used in commercial PDH technologies have significant drawbacks, such as the high cost and difficult reactivation of the platinum catalyst and the negative environmental impact of chromium pollution [11].

Quite naturally, there is great interest in developing competitive PDH catalysts that do not contain precious metals and chromium. The most promising of them encompass a variety of transition metal oxides, namely CoO_x, VO_x, GaO_x, MoO_x, FeO_x, WO_x, InO_x, ZnO, ZrO_2 and TiO_2, deposited on silica, alumina, zeolites and other oxide carriers [2–10,12,13]. The cobalt-containing catalysts should be especially highlighted because of their significant activity, relative affordability and moderate toxicity. In addition, carbon-based materials enriched with cobalt have also shown considerable potential in PDH [14–20]. However, remarkably, it is still not clear what structural motif in the cobalt catalysts promotes the PDH reaction. According to major conflicting opinions, Co^{+2} oxide

forms, rather than metallic cobalt (Co^0), and vice versa, may actually be the active sites [21–43]. As a compromise, some authors attribute catalytic activity to both oxidation states, Co^{+2} and Co^0 [33,35], or conclude that "the true active cobalt species for propane production are from tetrahedral Co^{+2} ions during the reaction" [21]. Additionally, apart from these possibilities, less attention has been drawn to the fact that low-valent first-row transition metal ions, including Co^{+1} in particular, can cause quite facile dehydrogenation of light alkanes [44–47]. Importantly, the oxidative addition/reductive elimination mechanism proposed for such reactions is independently well documented for a wide range of C–H bond functionalizations involving Co^{+1} organometallic compounds [48]. And lastly, atomically dispersed cobalt–nitrogen complexes deposited on carbon have also been suggested as possible catalytically active sites in the case of PDH over Co-N-C composites [14–20].

Given the strong interest in the activity of cobalt oxides in PDH, and cobalt–aluminum oxides in particular [21–23,26,28,29,33,34,41,43], we describe here a study on the behavior of $CoAl_2O_4$-Al_2O_3 catalysts in this reaction with the aim of elucidating the contributions of a variety of potential catalytic sites to catalytic performance.

2. Results

2.1. Catalyst Characterization

A number of textural characteristics of the $CoAl_2O_4$-Al_2O_3 catalysts, designated as CoAl-X (where X is the estimated molar ratio of Co/Al), are summarized in Table 1. The BET surface area was the highest for as-prepared CoAl-0.1 (291 m^2 g^{-1}), which is comparable to that of CoAl-0.05 (274 m^2 g^{-1}), despite the varying cobalt content, namely 6.7 and 4.3%, respectively. In addition, the total pore volume gradually increased as the cobalt content decreased. However, the BET surface areas and likewise the pore volumes of the spent–regenerated samples CoAl-0.25-R and CoAl-0.1-R were reduced markedly.

Table 1. Textural properties of the catalysts.

	Catalyst	Co/Al [1]	Co (wt%) [2]	S_{BET} (m^2 g^{-1})	Pore Size (nm)	V_{total} (cm^3 g^{-1})
1	CoAl-0.5	1:2	28.8	152	12.9	0.49
2	CoAl-0.25	1:4	17.0	219	16.5	0.90
3	CoAl-0.25-R [3]	1:4	13.2	137	21.7	0.74
4	CoAl-0.1	1:10	6.7	291	14.8	1.07
5	CoAl-0.1-R [3]	1:10	6.9	191	19.0	0.91
6	CoAl-0.05	1:20	4.3	274	16.3	1.12
7	Co/Al$_2$O$_3$	-	3.8	177	6.0	0.26
8	Al$_2$O$_3$	-	-	166	7.3	0.30

[1] The molar ratio of $Co(NO_3)_2$ and $Al(NO_3)_3$ taken for the catalyst preparation. [2] Determined by ICP. [3] The spent–regenerated (re-oxidized) catalyst.

The XRD patterns of as-synthesized and spent–regenerated catalysts allowed us to estimate the relative contributions of cobalt oxide and aluminum oxide crystalline phases (Figure 1). Table S1 summarizes the results of refining the structure of these samples. As expected, the peaks of Co_3O_4 form for CoAl-0.5, CoAl-0.25 and spent–regenerated CoAl-0.25-R catalysts were much stronger than for other catalysts. It is noteworthy that the crystallinity level of Co_3O_4 in the CoAl-0.25-R sample increased, whereas in the case of the CoAl-0.1-R catalyst the opposite occurred (Table S1). In general, the XRD data show that only CoAl-0.05, CoAl-0.1 and CoAl-0.1-R samples demonstrated the clear domination of a mixed Co−Al oxide crystalline form, which can be related to a separate $CoAl_2O_4$ spinel structure.
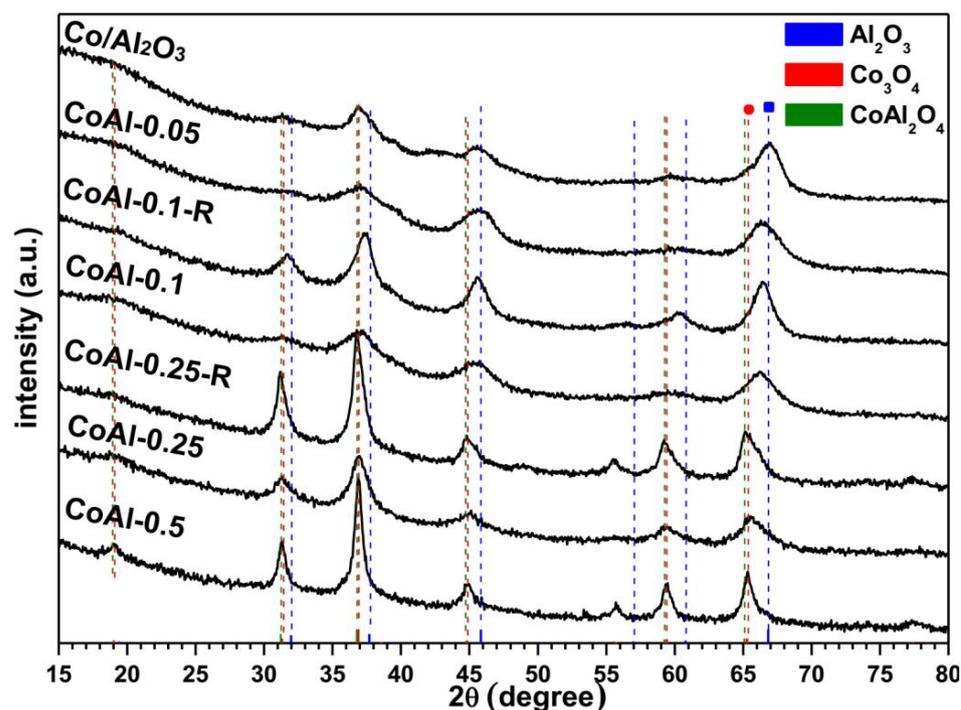
Figure 1. Powder XRD patterns of as-synthesized and spent–regenerated catalysts.

Figure 2 shows the H_2-TPR profiles of the catalysts, revealing that only CoAl-0.5, CoAl-0.25 and Co/Al$_2$O$_3$ exhibited a substantial H_2 uptake. For these catalysts, the reduction temperature of the first peak attributed to the reduction of Co$_3$O$_4$ to CoO was about 500 °C, which is notably higher than that of bulk Co$_3$O$_4$ (200–400 °C [37,38]) due to the strong interaction of Co$_3$O$_4$ with Al$_2$O$_3$, which prevents the catalyst reduction. The second reduction peak is located between 550 and 750 °C. Overall, the two-step reduction process corresponds to sequential CoO$_x$ reduction into CoO and then into Co^0 states of cobalt. The increased reduction temperature indicates that CoO$_x$ is tightly bound to the Al$_2$O$_3$ surface or forms a mixed oxide with it [37,38]. The weak hydrogen uptake for other catalysts (at least up to 600 °C and even higher) shows that their reduction is notably hindered, and the cobalt oxide phase remains largely resistant to reduction to a metal state.
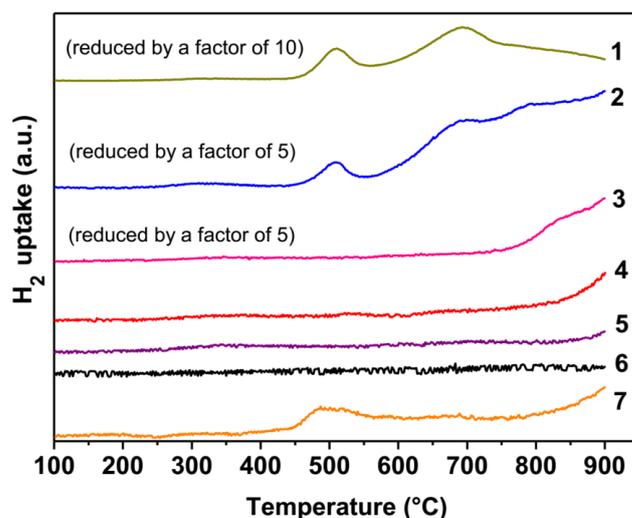

Figure 2. H_2-TPR profiles of (**1**) CoAl-0.5, (**2**) CoAl-0.25, (**3**) CoAl-0.25-R, (**4**) CoAl-0.1, (**5**) CoAl-0.1-R, (**6**) CoAl-0.05 and (**7**) Co/Al$_2$O$_3$ catalysts.

According to TEM data (Figure 3), the CoAl-0.1 sample consists mainly of a separate phase of cobalt aluminate $CoAl_2O_4$ (Figure 3b). In addition, the catalyst contains Al_2O_3 crystals, which are uniformly covered by CoO_x particles with a size of about 1–2 nm (Figure 3c). Notably, in Figure 3c the white particles are attributed to cobalt based on the relative mass (atomic number) of scattering Co and Al atoms, which affect the HAADF signal differently. In contrast, CoAl-0.25 contains, in addition to the above-mentioned species, well-distinguishable particles with an average grain size of 10–20 nm that can be assigned to both $CoAl_2O_4$ and Co_3O_4, taking into account their close lattice parameters (Figure 4).
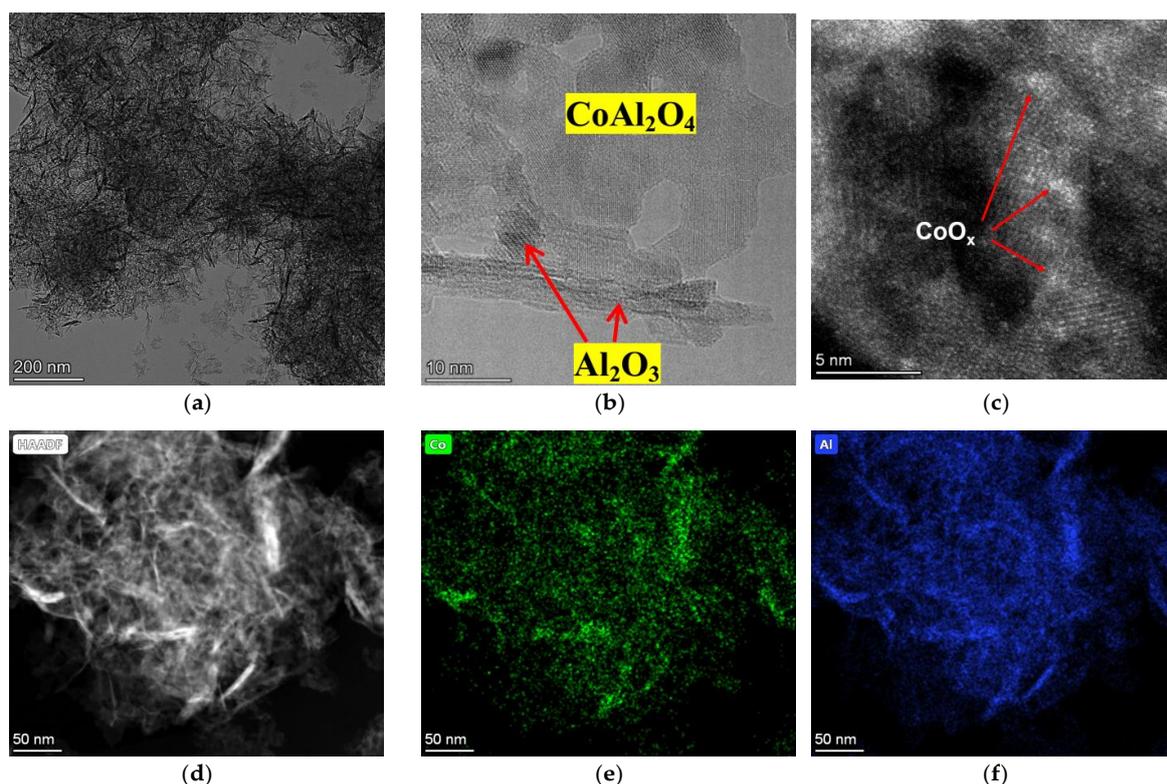

Figure 3. (**a**,**b**) TEM, (**c**,**d**) HAADF-STEM and (**e**,**f**) related EDX-STEM Co and Al elemental mapping images of as-synthesized CoAl-0.1 catalyst.
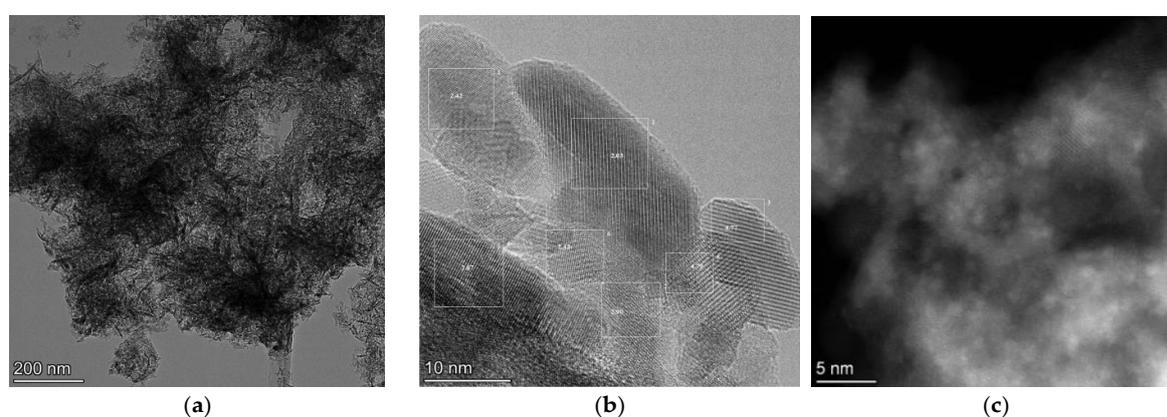

Figure 4. Low- (**a**) and higher- (**b**) magnification TEM and (**c**) HAADF-STEM images of as-synthesized CoAl-0.25 catalyst, representing a variety of phases, such as crystalline alumina, cobalt aluminate and cobalt oxides (including small particles on alumina).

To further characterize the nature of cobalt in the catalysts, the XPS spectra were obtained (Figure 5 and Table S2). In the high-resolution Co 2p spectra, the peaks centered at

781.3–781.8 (Co $2p_{3/2}$) and ~795 eV (Co $2p_{1/2}$) are related to Co^{2+} (Figure 5). An associated Co^{2+} satellite peak (shake-up peak) centered at ~787.0 eV is also present, confirming the predominant state of cobalt as tetrahedral Co^{2+} ions. As expected, the Al 2p and O 1s spectra of the catalysts are very similar, confirming the lack of differentiation in the electron state of aluminum and oxygen among the catalysts.
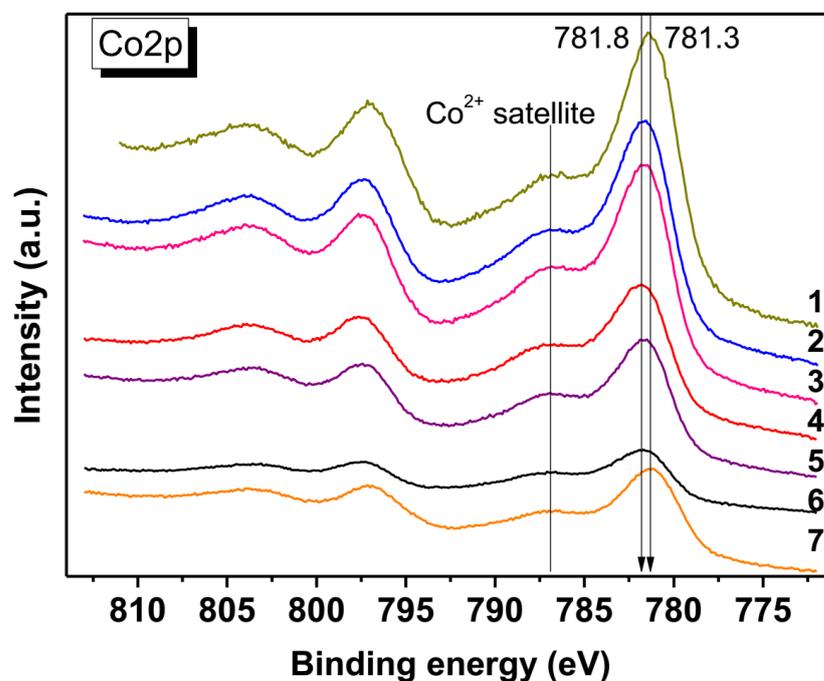

Figure 5. High-resolution Co 2p XPS spectra of (**1**) CoAl-0.5, (**2**) CoAl-0.25, (**3**) CoAl-0.25-R, (**4**) CoAl-0.1, (**5**) CoAl-0.1-R, (**6**) CoAl-0.05 and (**7**) Co/Al_2O_3 catalysts.

2.2. Gas-Phase Catalytic Reactions of Propane in a Flow Reactor

The activity of CoAl catalysts in PDH was estimated at 600 °C using a 10% propane/N_2 mixture. Unlike other samples, CoAl-0.5 proved unsuitable to catalyze PDH, as it was prone to rapid carbonization, clogging the reactor. This applies to both the fresh and spent–regenerated catalysts, and can be explained by the presence of the relatively high content of an easily reduced massive CoO_x form, which tends to induce cracking reactions [35,37–40]. In contrast, fresh CoAl-0.1 and CoAl-0.05 catalysts provided 47 and 36% of propane conversion after a 20 and 30 min induction period, respectively (Figure 6). Then, there was a gradual decrease in catalytic activity, while the selectivity to propylene remained at the initial level of ca. 95%. It is noteworthy that despite the two-and-a-half-times-higher Co content in the CoAl-0.25 catalyst (Table 1), its activity was nevertheless comparable to that of CoAl-0.1 (Figure 6). However, the induction period for CoAl-0.25 was twice as long, whereas selectivity to propylene was notably lower, reaching 90% only at 1.5 h. This result illustrates that the readily reducible extra-framework CoO_x species still present in the fresh CoAl-0.25 catalyst impairs the target catalytic performance.

It should be noticed that under the specified reaction conditions, especially during the induction period, propane underwent concurrent cracking reactions yielding mainly methane, along with carbonaceous material (see below), which is typical for high-temperature PDH [2–10].

The pre-treatment of the fresh CoAl-0.1 catalyst with hydrogen (as described in Section 4.5) shortened the induction period and led to a slight increase in the maximal propane conversion (Figure 7). However, regeneration of the spent CoAl-0.1 catalyst by high-temperature treatment with oxygen (Section 4.5) reduced its activity by about 20% compared to the fresh catalyst (Figure 7a). On the other hand, the selectivity to propylene increased to 96% (Figure 7b). The same is true of the spent–regenerated CoAl-0.25-R cata-

lyst, which provided notably higher selectivity to propylene, a shorter induction period, and well-reproducible catalytic activity tested in several runs (Figure 8).
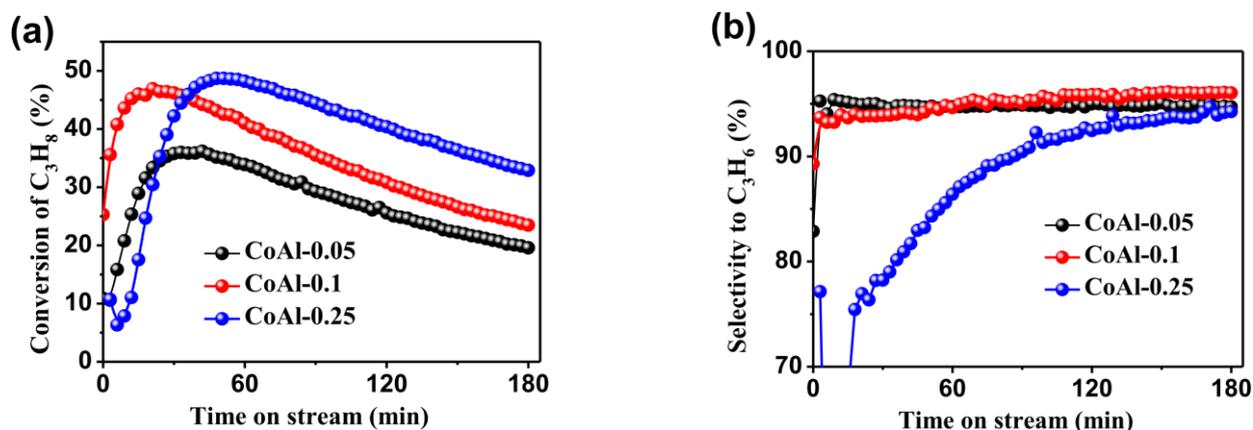

Figure 6. Propane conversion (**a**) and selectivity to propylene (**b**) as functions of time on stream over CoAl catalysts at T = 600 °C and P = 1 atm. Gas mixture: 10 vol.% propane, N_2 balance; GHSV = 7500 mL h^{-1} g_{cat}^{-1}.
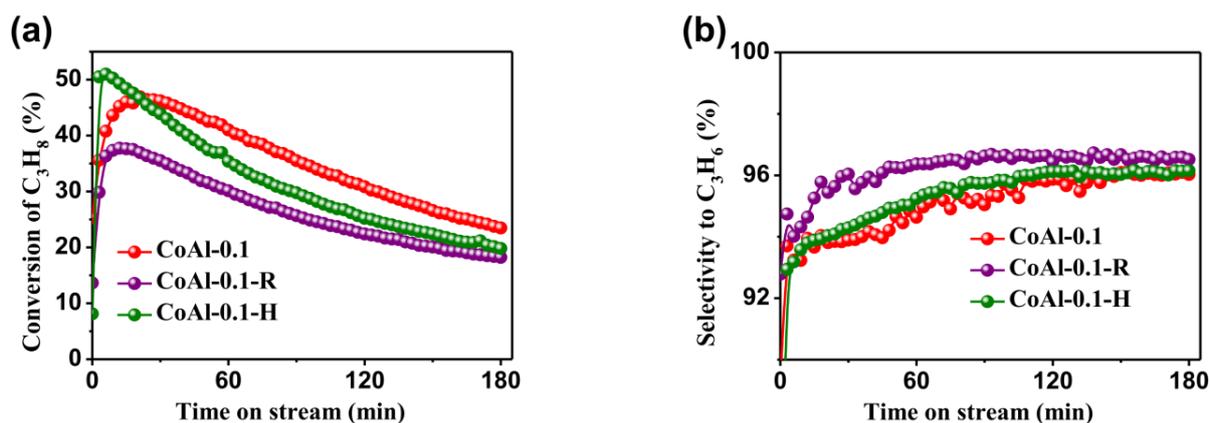

Figure 7. Propane conversion (**a**) and selectivity to propylene (**b**) as functions of time on stream over CoAl-0.1, CoAl-0.1-R (spent–regenerated) and CoAl-0.1-H (pre-treated with H_2) catalysts at T = 600 °C and P = 1 atm. Gas mixture: 10 vol.% propane, N_2 balance; GHSV = 7500 mL h^{-1} g_{cat}^{-1}.
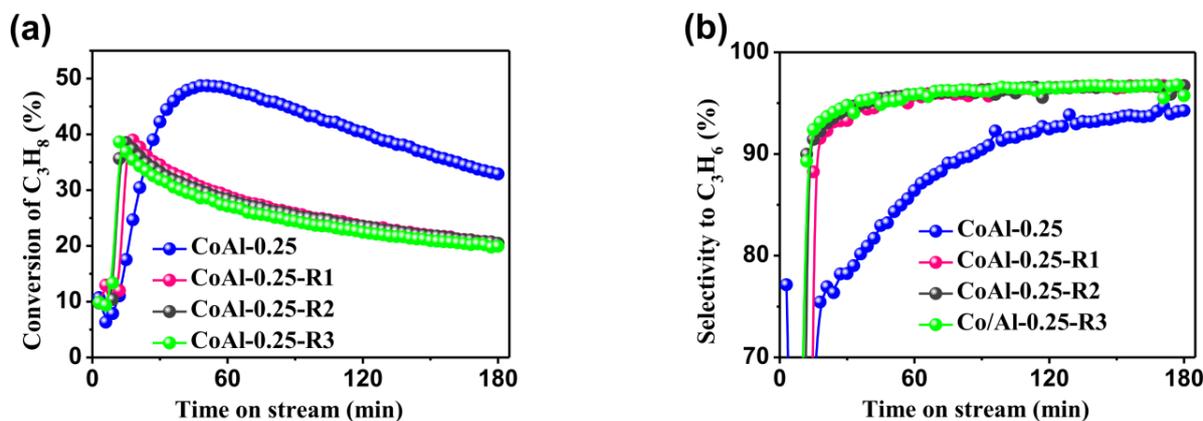

Figure 8. Propane conversion (**a**) and selectivity to propylene (**b**) as functions of time on stream over CoAl-0.25 and spent–regenerated CoAl-0.25-RN catalysts (where N is the execution number) at T = 600 °C and P = 1 atm. Gas mixture: 10 vol.% propane, N_2 balance; GHSV = 7500 mL h^{-1} g_{cat}^{-1}.

Furthermore, the catalytic properties of the "reference" Co/Al_2O_3 sample turned out to be comparable with that of CoAl-0.05 (Figure S1). This is not surprising, taking into account the close content of cobalt (Table 1), while the other characteristics of these catalysts are somewhat different. The selectivity to propylene over Co/Al_2O_3 was even the highest among the tested catalysts, reaching 97% and 98% for fresh and spent–regenerated samples, respectively (Figure S2). However, the relative drop in maximal propane conversion (from 36 to 25%) after the catalyst regeneration was the most significant (Figure S2).

2.3. Structural Changes in Catalysts during PDH and Subsequent Regeneration

According to the literature, the deactivation of cobalt-containing catalysts during PDH is commonly due to the deposition of coke and the restructuring of cobalt species under high-temperature reducing conditions [19,20,28,29]. Indeed, the microscopic images of the spent CoAl-0.1 catalyst show considerable growth of carbon nanotubes (Figure 9a,b). However, encapsulation of Co-Al oxides in carbon did not occur (cf. [19,20]), which means that carbonization by itself is not a cause of deactivation. More important is the fact of partial reduction of cobalt to the metallic state with the formation of Co nanoparticles of relatively large sizes about 10 nm (Figure 9b,d,e), although small particles of Co on alumina did not undergo substantial aggregation (Figure 9c).

Figure 9. (**a**,**b**) TEM, (**c**,**d**) HAADF-STEM and (**e**,**f**) related EDX-STEM Co and Al elemental mapping images of the spent CoAl-0.1 catalyst (after 3 h of operation at T = 600 °C and P = 1 atm for the gas mixture of 10 vol% propane, N_2 balance, GHSV = 7500 mL h^{-1} g_{cat}^{-1}).

Regeneration of the CoAl-0.1 spent catalyst by high-temperature treatment with molecular oxygen results in the redispersion of aggregated cobalt nanoparticles, providing a

catalyst quite similar in appearance to the original (Figure 10). The CoAl-0.25 catalyst also restores its structure after the use in PDH and subsequent heat treatment in oxygen, although more significant differentiation in CoAl-0.25-R morphology has occurred. Thus, separate phases of alumina (weakly enriched with cobalt), cobalt aluminate and rather large particles of Co_3O_4 can be observed via TEM (Figures S3 and S4). Remarkably, according to H_2-TPR data, the CoO_x species in CoAl-0.25-R are not so readily reducible with hydrogen, as was found for CoO_x in the fresh CoAl-0.25 catalyst (Figure 2).
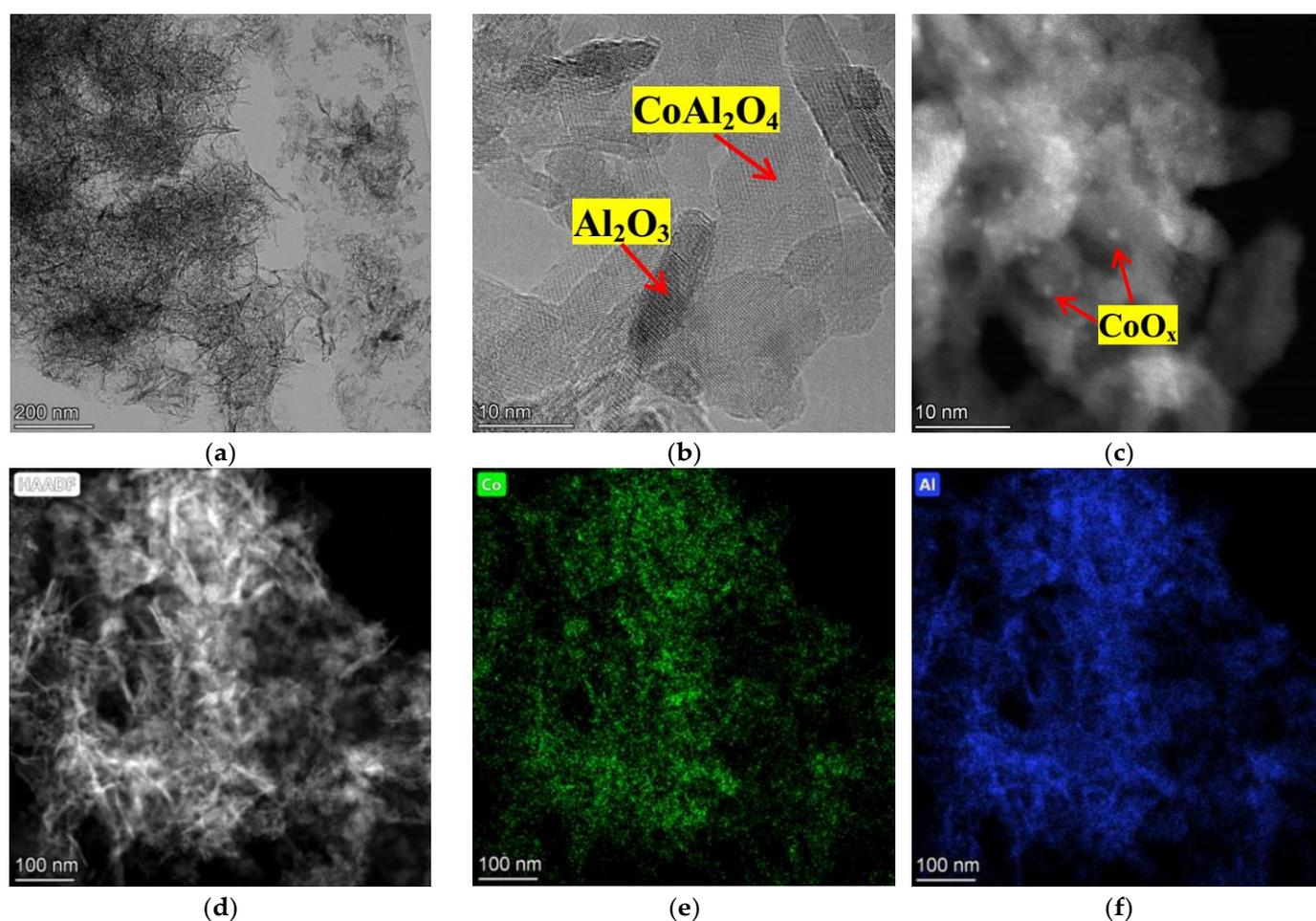

Figure 10. (**a**,**b**) TEM, (**c**,**d**) HAADF-STEM and (**e**,**f**) related EDX-STEM Co and Al elemental mapping images of the spent–regenerated CoAl-0.1-R catalyst.

3. Discussion

The CoAl-0.1 sample, which demonstrated the best catalytic performance in PDH, comprises three structural elements: Al_2O_3, small CoO_x particles (in the size range of 1–2 nm) on its surface and adjacent areas of crystalline cobalt aluminate ($CoAl_2O_4$). The CoAl-0.25 catalyst, exhibiting comparable catalytic activity, contains, in addition, Co_3O_4 particles of about 10 nm size and the Co_3O_4 phase of a comparatively low crystallinity (XRD data, Figure 1). The latter phase was easily reduced and could be responsible for the lower selectivity to propylene and longer induction period compared to the CoAl-0.1 catalyst. Indeed, CoAl-0.25-R, showing better selectivity to propylene and a shortened induction period (Figure 8), differed from CoAl-0.25 through its increased Co_3O_4 particle size (up to 100 nm, Figure S4) and their increased crystallinity (Figure 1, Table S1). Additionally, CoAl-0.25-R became practically non-reducible with hydrogen until reaching 700 °C (Figure 2). Furthermore, the high-temperature treatment with oxygen of both of the

spent CoAl-0.1 and CoAl-0.25 catalysts resulted in a marked decrease in specific surface area (Table 1), which may be one of the reasons for the partial loss of their activity.

It is obvious that the target activity of CoAl catalysts in PDH may be associated with the small CoO_x particles on alumina, as well as with comparatively large and slowly reducible $CoAl_2O_4$ and Co_3O_4 crystalline phases, which can undergo a common evolutionary chain during PDH or pre-reduction with hydrogen: $Co^{+2/+3} \rightarrow$ framework $Co^{+2} \rightarrow$ isolated Co^0 $\rightarrow$ small-size $(Co^0\text{-}Co^0)_n$ cluster $\rightarrow$ large cobalt particle (cf. [35–39]). Among these forms, as mentioned in Section 1, Co^{+2} oxides and/or small Co^0 species are widely suggested to be the active catalytic sites [21–43].

It is noteworthy that the basic rationale for the key contribution of tetrahedral Co^{+2} ions is their exclusive observation by physical–chemical techniques with no detection of Co^0 under PDH conditions [21–36]. The proposed reaction mechanism suggests a non-redox pathway involving the heterolytic C–H bond cleavage over four-coordinated Co^{+2} incorporated in the framework of oxide support [25,36]. In contrast, extra-framework Co_3O_4 weakly bonded to the support (if present) can easily be reduced to comparatively large metallic cobalt particles [35,37–40], leading to propane cracking until these zones are strongly carbonized [19–22,33].
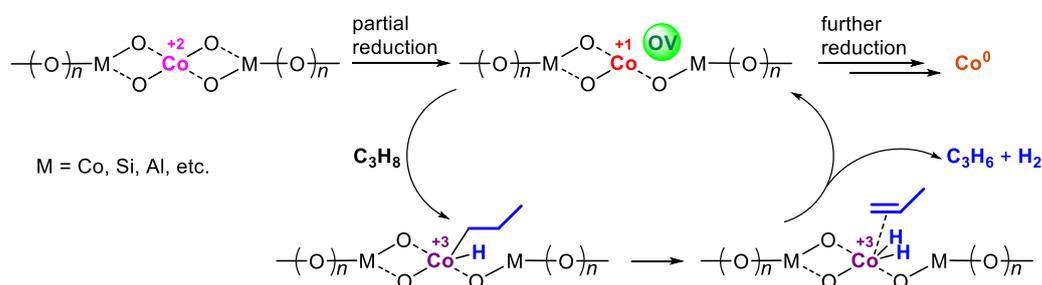
However, equally convincing is the evidence that well-dispersed Co^0 species generated in situ by partial reduction of Co^{+2} ions are the alternative active catalytic sites [33,35,40–42]. The main argument here is based on the apparent relationship between the appearance of cobalt nanoparticles and the increase in catalytic activity. Furthermore, Kondratenko et al. have shown recently that propylene formation depends linearly on Co^0 accumulation in Co/silicalite-1 catalysts [43]. Though perhaps, the catalytic activity could simply correlate with the steady reduction of Co^{+2} to Co^0 due to a related but different process.

With regard to the CoAl catalytic system, it should be noted that the most effective PDH catalysts, such as CoAl-0.05, CoAl-0.1, CoAl-0.1-R and CoAl-0.25-R, are actually most resistant to reduction (metallization) by hydrogen (Figure 2). Moreover, a slow reduction of CoO_x to metallic cobalt followed by its aggregation to cobalt nanoparticles (Figure 9b) is accompanied by the catalyst's progressive deactivation, which may be related. On the other hand, the key catalytic activity of four-coordinated Co^{+2} ions only (whether they are part of CoO_x particles on aluminum or are included in $CoAl_2O_4$ and Co_3O_4 crystals) cannot explain the results of numerous case studies where a definite relationship between of the catalytic activity and Co^0 accumulation was found. Nevertheless, this apparent contradiction can be resolved by examining the missing link between the cobalt states Co^{+2} and Co^0 under the PDH reaction.

Indeed, a close literary analogy of the process of nickel(II) oxide reduction by hydrogen reveals that NiO(100) crystals exhibiting negligible reactivity to H_2 become active in splitting H–H bonds when surface defects, namely O vacancies (OVs), are created [49–51]. Remarkably, a correlation was found between the concentration of OVs and the rate of NiO reduction to Ni^0 [49]. It seems reasonable that a similar process of OV generation occurs on the surface of tetrahedral Co^{+2} oxide forms in the course of PDH. The lattice oxygen consumption leading to the formation of OVs under conditions of thermal gaseous reduction is quite typical for transition metal oxides, including CoO_x [52–55]. Moreover, the importance of OVs for efficient C−H bond activation in PDH has already been proven for a number of metal oxides, such as CeO_2 [56] and TiO_2 [57,58], and even for "non-reducible" oxides, such as ZrO_2 [59] and Al_2O_3 [60]. Likewise, the catalytic activity of WO_3 in PDH, provided by pre-treatment with hydrogen, may have an analogous origin [61].

The involvement of OVs could explain the induction period normally required for PDH catalyzed by cobalt oxides, the positive effect of pre-reduction with hydrogen (see, for example, Figure 7) and the observed correlation of catalytic activity with Co^0 accumulation, while an overly extensive reduction of Co^{+2} to Co^0 causes catalyst deactivation. Also notably, Co atoms surrounding OVs and carrying uncompensated positive charge can actually simulate Co^{+1} species able to catalyze PDH through the oxidative addi-

tion/reductive elimination pathway (Scheme 1), thus linking together the Co^{+2}, Co^{+1} and Co^0 forms, considered earlier as alternatives in the literature.

Scheme 1. Probable mechanism of PDH involving OVs generated on the surface of tetrahedral Co^{+2} oxide forms.

Summarizing the above considerations, nanocrystalline $CoAl_2O_4$ and Co_3O_4, as well as fine CoO_x particles on alumina (all present in CoAl active catalysts) may exhibit the same catalytic properties due to similar evolution under PDH conditions, namely partial reduction to metallic cobalt (ultimately) through the intermediacy of surface OVs. The small content of cobalt in CoAl catalysts ensures their strong interaction with alumina and embedding in the spinel structure, which generally prevents deep reduction of CoO_x to Co^0 under PDH conditions and provides the catalyst's relative stability. Based on these assumptions, progress in the design of cobalt-containing catalysts and similar transition metal oxide catalytic systems will require their optimal ability to generate surface Ovs, along with their resistance to subsequent reduction and metallization to be taken into account.

4. Materials and Methods

4.1. Materials

Cobalt(II) nitrate hexahydrate ($Co(NO_3)_2 \cdot 6H_2O$, ≥98%, Fisher Scientific UK, Loughborough, UK) and aluminum nitrate nonahydrate ($Al(NO_3)_3 \cdot 9H_2O$, ≥98%, Sigma-Aldrich, Merck Life Science LLC, Moscow, Russia) were used as received from the chemical suppliers.

4.2. Catalyst Preparation

The cobalt aluminate spinels ($CoAl_2O_4$-Al_2O_3) were obtained by mixing 2 M $Co(NO_3)_2$ and 2 M $Al(NO_3)_3$ aqueous solutions followed by co-precipitating with a 12.5% NH_4OH at constant pH 7.5 and temperature of 70 °C. The resulting precipitates were filtered and washed with distilled water until the ammonia was removed. The obtained materials were dried to an air-dry state at room temperature, then at 110 °C for 12 h, and calcined in air at 650 °C for 4 h in a muffle furnace. Accordingly, based on the molar ratio of cobalt and aluminum salts taken, the catalyst samples, denoted as CoAl-0.5, CoAl-0.25, CoAl-0.1 and CoAl-0.05, were prepared in the amount of 50 g each (Table 1).

The Co/Al_2O_3 catalyst was prepared via the incipient wetness impregnation of γ-Al_2O_3 with a cobalt(II) nitrate solution followed by drying at 110 °C for 12 h and thermal treatment in air at 650 °C for 4 h.

4.3. Catalyst Characterization Techniques

The X-ray diffraction (XRD) data were obtained on the diffractometer ARL X'tra (Thermo Fisher Scientific, Waltham, MA, USA) using monochromatic CuKα radiation (λ = 1.5418 Å) in a range of 2θ = 15−80° with a step of 0.02° (1°/min) using linear detector Mython2R 1D (Dectris, Baden-Daettwil, Switzerland) with an angle of 7.0°. Refinement of the lattice parameters and determination of average crystallite sizes and weight ratios of Co_3O_4/Al_2O_3 were carried out by the Rietveld method applied for a range of 2θ = 63−70° using the TOPAS 4.2 program and structural data from the ICSD database (Table S1).

Temperature-programmed reduction (H_2-TPR) was performed in a flow system with a thermal conductivity detector. The samples (0.05 g, 0.25–0.5 mm fraction) were heated at

rates of 10 °C min^{-1} to 900 °C; the flow rate of the reducing mixture (10% H$_2$ in argon) was 40 cm^3 min^{-1}.

The porous structure parameters were determined from N$_2$ adsorption isotherms at 77 K on an ASAP-2400 (Micromeritics, Norcross, GA, USA) analyzer after degassing the samples at 150 °C to a residual pressure of 30 mTorr (4 Pa).

The content of Co element in the samples was measured with an Optima 4300 DV inductively coupled plasma optical emission spectrometer (ICP-OES) (PerkinElmer, Wellesley, MA, USA).

High-resolution transmission electron microscopy (HRTEM) and scanning transmission electron microscopy (STEM) were conducted with a Themis Z (Thermo Fisher Scientific, Waltham, MA, USA) instrument with an accelerating voltage of 200 kV and lattice resolution of 0.07 nm. The TEM images were recorded with a Ceta 16 (Thermo Fisher Scientific, USA) CCD matrix. Elemental analysis was performed with a Super-X EDS detector (Thermo Fisher Scientific, USA). High-angle annular dark-field (HAADF) STEM images were recorded using a standard ThemisZ detector.

X-ray photoelectron spectra (XPS) were recorded on a SPECS (Berlin, Germany) photoelectron spectrometer using a hemispherical PHOIBOS-150-MCD-9 analyzer (Al Kα radiation, hν = 1486.6 eV, 150 W). The binding energy (BE) scale was pre-calibrated using the positions of the peaks of Au 4f$_{7/2}$ (BE = 84.0 eV) and Cu 2p$_{3/2}$ (BE = 932.67 eV) core levels. The BE values were corrected by reference to the C 1s internal standard (284.5 eV).

4.4. Catalytic Performance Tests

The PDH reactions were carried out at atmospheric pressure in a 7.5 mm quartz tube reactor loaded with a catalyst (0.2 g, 0.25–0.5 mm fraction), mixed with 1 mL quartz particles (d = 0.45 to 1 mm). The gas mixture (10 vol% propane balanced with nitrogen) was fed to the reactor at a gas hourly space velocity (GHSV) of 7500 mL h^{-1} g$_{cat}$$^{-1}$ (propane weight hourly space velocity of 1.4 h^{-1}). The reaction temperature, 600 °C, was controlled inside the reactor with an accuracy of ±0.5 °C. The reaction products were analyzed by an online gas chromatograph (Chromos GC-1000, Chromos Engineering, Dzerzhinsk, Russia) with a flame ionization detector, using a quartz capillary column of an inner diameter of 0.32 mm and a length of 7 m. The column was prepared by the static high-pressure method, yielding a monolithic layer of porous SiO$_2$ formed in the process of sol-gel synthesis directly inside the capillary [62]. Prior to the measurements, the catalysts were heated at 600 °C in a flow of N$_2$ for 1 h. The blank experiment (the Al$_2$O$_3$/ quartz particles only) showed propane conversion of ~1.2% and selectivity to propylene of about 70%.

The propane conversion (X) and propylene selectivity (S) were calculated according to the carbon atom balance method:

$$X_{C_3H_8} = \frac{C^0_{C_3H_8} - C_{C_3H_8}}{C^0_{C_3H_8}} \times 100\%;$$

$$S_{C_3H_6} = \frac{C_{C_3H_6}}{C^0_{C_3H_8} - C_{C_3H_8}} \times 100\%;$$

where $C_{C_3H_8}$ and $C_{C_3H_6}$ are the mole flow rates of propane and propylene, respectively. In view of the reaction-induced changes in the gas flow due to the conversion of one molecule of propane into two molecules (propylene and hydrogen) during the reaction, the values of $C_{C_3H_8}$ and $C_{C_3H_6}$ were normalized by carbon balance accordingly.

4.5. Catalyst Pre-Reduction with H$_2$ and Regeneration Procedures

The treatment of CoAl catalysts with hydrogen was carried out in the reactor at 600 °C in the H$_2$ flow (15 mL min^{-1}) for 1.5 h and then in the N$_2$ flow (30 mL min^{-1}) for 1 h.

After catalytic testing in PDH, the spent CoAl catalysts were treated in the reactor at 600 °C in the O$_2$ flow (15 mL min^{-1}) for 1.5 h and then in the N$_2$ flow (30 mL min^{-1}) for 1 h.

5. Conclusions

It was shown that cobalt aluminate containing 4–7 wt.% Co, and as a consequence, consisting mainly of alumina (with inclusions of small CoO_x particles on the surface) and $CoAl_2O_4$ spinel crystallites, can be an effective catalyst for PDH reactions under practical operating conditions (600 °C, 1 atm). Further increasing the Co content to 17 wt.% resulted in the formation of an additional Co_3O_4 phase without increasing the catalyst efficiency towards PDH.

The catalysts' loss of activity with time on stream is related to cobalt aggregation in the form of metallic Co nanoparticles; however, coke deposition, largely in the form of carbon nanotubes, does not appear to be the critical reason for the catalysts' deactivation. The high-temperature treatment of spent catalysts with molecular oxygen leads to their regeneration with a partial decrease in activity, but at the same time is accompanied by the stabilization of the catalysts' operation.

The structural motifs, such as tetrahedral Co^{2+} species located in the $CoAl_2O_4$ and Co_3O_4 spinel forms, as well as in the small CoO_x particles tightly covering alumina, can be regarded as the feasible primary active-site ensembles. However, their subsequent evolution under PDH reaction conditions, consisting of a partial reduction to metallic cobalt through the intermediacy of surface OVs, may provide further rationale for the origin of the catalytic activity of cobalt aluminates in PDH.

Supplementary Materials: The following supporting information can be downloaded at: https://www.mdpi.com/article/10.3390/catal13111419/s1, Table S1: Grid parameters (a), average crystallite sizes and weight ratios; Figure S1: Propane conversion and selectivity to propylene as functions of time on stream over CoAl and Co/Al_2O_3 catalysts; Figure S2: Propane conversion and selectivity to propylene as functions of time on stream over Co/Al_2O_3 and Co/Al_2O_3-R catalysts; Figure S3: Low- and higher-magnification TEM images of the spent–regenerated CoAl-0.25-R catalyst; Figure S4: HAADF-STEM and related EDX-STEM Co and Al elemental mapping images of different areas of CoAl-0.25-R; Table S2: High-resolution XPS spectra of Al 2p and O 1s of the samples; Table S3: The N_2 adsorption/desorption isotherms and the pore size distribution of the samples.

Author Contributions: Conceptualization, A.N.C.; investigation, A.N.C., S.V.C., E.Y.G., I.P.P., G.A.Z., A.S.G. and A.A.S.; data curation, K.Y.K. and V.I.S.; writing—original draft preparation, K.Y.K.; writing—review and editing, K.Y.K. and V.I.S.; supervision, V.I.S. All authors have read and agreed to the published version of the manuscript.

Data Availability Statement: Not applicable.

Conflicts of Interest: The authors declare no conflict of interest.

References

1. Zimmermann, H. Propene. In *Ullmann's Encyclopedia of Industrial Chemistry*; Wiley-VCH Verlag GmbH & Co., KGaA: Weinheim, Germany, 2013. [CrossRef]
2. Sattler, J.J.H.B.; Ruiz-Martinez, J.; Santillan-Jimenez, E.; Weckhuysen, B.M. Catalytic dehydrogenation of light alkanes on metals and metal oxides. *Chem. Rev.* **2014**, *114*, 10613–10653. [CrossRef] [PubMed]
3. Hu, Z.-P.; Yang, D.; Wang, Z.; Yuan, Z.-Y. State-of-the-art catalysts for direct dehydrogenation of propane to propylene. *Chin. J. Catal.* **2019**, *40*, 1233–1254. [CrossRef]
4. Martino, M.; Meloni, E.; Festa, G.; Palma, V. Propylene Synthesis: Recent Advances in the Use of Pt-Based Catalysts for Propane Dehydrogenation Reaction. *Catalysts* **2021**, *11*, 1070. [CrossRef]
5. Dong, S.; Altvater, N.R.; Mark, L.O.; Hermans, I. Assessment and comparison of ordered & non-ordered supported metal oxide catalysts for upgrading propane to propylene. *Appl. Catal. A-Gen.* **2021**, *617*, 118121. [CrossRef]
6. Chen, S.; Chang, X.; Sun, G.; Zhang, T.; Xu, Y.; Wang, Y.; Pei, C.; Gong, J. Propane dehydrogenation: Catalyst development, new chemistry, and emerging technologies. *Chem. Soc. Rev.* **2021**, *50*, 3315–3354. [CrossRef] [PubMed]

7.　Otroshchenko, T.; Jiang, G.; Kondratenko, V.A.; Rodemerck, U.; Kondratenko, E.V. Current status and perspectives in oxidative, non-oxidative and CO_2-mediated dehydrogenation of propane and isobutane over metal oxide catalysts. *Chem. Soc. Rev.* **2021**, *50*, 473–527. [CrossRef]

8.　Dai, Y.; Gao, X.; Wang, Q.; Wan, X.; Zhou, C.; Yang, Y. Recent progress in heterogeneous metal and metal oxide catalysts for direct dehydrogenation of ethane and propane. *Chem. Soc. Rev.* **2021**, *50*, 5590–5630. [CrossRef]

9.　Wang, Y.; Hu, P.; Yang, J.; Zhu, Y.-A.; Chen, D. C–H bond activation in light alkanes: A theoretical perspective. *Chem. Soc. Rev.* **2021**, *50*, 4299–4358. [CrossRef]

10.　Liu, S.; Zhang, B.; Liu, G. Metal-based catalysts for the non-oxidative dehydrogenation of light alkanes to light olefins. *React. Chem. Eng.* **2021**, *6*, 9–26. [CrossRef]

11.　Phung, T.K.; Pham, T.L.M.; Vu, K.B.; Busca, G. (Bio)Propylene production processes: A critical review. *J. Environ. Chem. Eng.* **2021**, *9*, 105673. [CrossRef]

12.　Yuan, Y.; Lee, J.S.; Lobo, R.F. Ga^+-Chabazite Zeolite: A Highly Selective Catalyst for Nonoxidative Propane Dehydrogenation. *J. Am. Chem. Soc.* **2022**, *144*, 15079–15092. [CrossRef]

13.　Yuan, Y.; Lobo, R.F. Zinc Speciation and Propane Dehydrogenation in Zn/H-ZSM-5 Catalysts. *ACS Catal.* **2023**, *13*, 4971–4984. [CrossRef]

14.　Xie, J.; Kammert, J.D.; Kaylor, N.; Zheng, J.W.; Choi, E.; Pham, H.N.; Sang, X.; Stavitski, E.; Attenkofer, K.; Unocic, R.R.; et al. Atomically Dispersed Co and Cu on N-Doped Carbon for Reactions Involving C–H Activation. *ACS Catal.* **2018**, *8*, 3875–3884. [CrossRef]

15.　Cao, T.; Dai, X.; Li, F.; Liu, W.; Bai, Y.; Fu, Y.; Qi, W. Efficient Non-Precious Metal Catalyst for Propane Dehydrogenation: Atomically Dispersed Cobalt-nitrogen Compounds on Carbon Nanotubes. *ChemCatChem* **2021**, *13*, 3067–3073. [CrossRef]

16.　Wang, Y.; Suo, Y.; Ren, J.-T.; Wang, Z.; Yuan, Z.-Y. Spatially isolated cobalt oxide sites derived from MOFs for direct propane dehydrogenation. *J. Colloid Interface Sci.* **2021**, *594*, 113–121. [CrossRef]

17.　Wang, Q.; Xu, W.; Ma, Z.; Yu, F.; Chen, Y.; Liao, H.; Wang, X.; Zhou, J. Highly Effective Direct Dehydrogenation of Propane to Propylene by Microwave Catalysis at Low Temperature over Co−Sn/NC Microwave Catalyst. *ChemCatChem* **2021**, *13*, 1009–1022. [CrossRef]

18.　Li, Y.-M.; Liu, Z.-Y.; Zhang, Q.-Y.; Wang, Y.-J.; Cui, G.-Q.; Zhao, Z.; Xu, C.-M.; Jiang, G.-Y. Influence of carbonization temperature on cobalt-based nitrogen-doped carbon nanopolyhedra derived from ZIF-67 for nonoxidative propane dehydrogenation. *Pet. Sci.* **2022**, *20*, 559–568. [CrossRef]

19.　Chernov, A.N.; Sobolev, V.I.; Koltunov, K.Y. Propane dehydrogenation to propylene over Co@N-doped carbon: Structure-activity-selectivity relationships. *Catal. Commun.* **2022**, *170*, 106495. [CrossRef]

20.　Chernov, A.N.; Sobolev, V.I.; Gerasimov, E.Y.; Koltunov, K.Y. Propane Dehydrogenation on Co-NC/SiO_2 Catalyst: The Role of Single-Atom Active Sites. *Catalysts* **2022**, *12*, 1262. [CrossRef]

21.　Sun, Y.; Wu, Y.; Shan, H.; Li, C. Studies on the Nature of Active Cobalt Species for the Production of Methane and Propylene in Catalytic Dehydrogenation of Propane. *Catal. Lett.* **2015**, *145*, 1413–1419. [CrossRef]

22.　Sun, Y.N.; Gao, Y.N.; Wu, Y.M.; Shan, H.H.; Wang, G.W.; Li, C.Y. Effect of sulfate addition on the performance of Co/Al_2O_3 catalysts in catalytic dehydrogenation of propane. *Catal. Commun.* **2015**, *60*, 42–45. [CrossRef]

23.　Li, W.; Yu, S.Y.; Meitzner, G.D.; Iglesia, E. Structure and Properties of Cobalt-Exchanged H-ZSM5 Catalysts for Dehydrogenation and Dehydrocyclization of Alkanes. *J. Phys. Chem. B* **2001**, *105*, 1176–1184. [CrossRef]

24.　Hu, B.; Getsoian, A.; Schweitzer, N.M.; Das, U.; Kim, H.; Niklas, J.; Poluektov, O.; Curtiss, L.A.; Stair, P.C.; Miller, J.T.; et al. Selective propane dehydrogenation with single-site Co-II on SiO_2 by a non-redox mechanism. *J. Catal.* **2015**, *322*, 24–37. [CrossRef]

25.　Estes, D.P.; Siddiqi, G.; Allouche, F.; Kovtunov, K.V.; Safonova, O.V.; Trigub, A.L.; Koptyug, I.V.; Coperet, C. C−H Activation on Co,O Sites: Isolated Surface Sites versus Molecular Analogs. *J. Am. Chem. Soc.* **2016**, *138*, 14987–14997. [CrossRef] [PubMed]

26.　Hu, B.; Kim, W.-G.; Sulmonetti, T.P.; Sarazen, M.L.; Tan, S.; So, J.; Liu, Y.; Dixit, R.S.; Nair, S.; Jones, C.W. A Mesoporous Cobalt Aluminate Spinel Catalyst for Nonoxidative Propane Dehydrogenation. *ChemCatChem* **2017**, *9*, 3330–3337. [CrossRef]

27.　Song, S.J.; Li, J.; Wu, Z.J.; Zhang, P.; Sun, Y.Q.; Song, W.Y.; Li, Z.X.; Liu, J. In situ encapsulated subnanometric CoO clusters within silicalite-1 zeolite for efficient propane dehydrogenation. *AIChE J.* **2022**, *68*, e17451. [CrossRef]

28.　Dewangan, N.; Ashok, J.; Sethia, M.; Das, S.; Pati, S.; Kus, H.; Kawi, S. Cobalt-Based Catalyst Supported on Different Morphologies of Alumina for Non-oxidative Propane Dehydrogenation: Effect of Metal Support Interaction and Lewis Acidic Sites. *ChemCatChem* **2019**, *11*, 4923–4934. [CrossRef]

29.　Dai, Y.; Gu, J.; Tian, S.; Wu, Y.; Chen, J.; Li, F.; Du, Y.; Peng, L.; Ding, W.; Yang, Y. $γ$-Al_2O_3 sheet-stabilized isolate Co^{2+} for catalytic propane dehydrogenation. *J. Catal.* **2020**, *381*, 482–492. [CrossRef]

30.　Bian, Z.F.; Dewangan, N.; Wang, Z.G.; Pati, S.; Xi, S.B.; Borgna, A.; Kus, H.; Kawi, S. Mesoporous-Silica-Stabilized Cobalt(II) Oxide Nanoclusters for Propane Dehydrogenation. *ACS Appl. Nano Mater.* **2021**, *4*, 1112–1125. [CrossRef]

31.　Wu, L.Z.; Ren, Z.Z.; He, Y.S.; Yang, M.; Yu, Y.K.; Liu, Y.M.; Tan, L.; Tang, Y. Atomically Dispersed Co^{2+} Sites Incorporated into a Silicalite-1 Zeolite Framework as a High Performance and Coking-Resistant Catalyst for Propane Nonoxidative Dehydrogenation to Propylene. *ACS Appl. Mater. Interfaces* **2021**, *13*, 48934–48948. [CrossRef]

32.　Ren, Z.; He, Y.; Yang, M.; Deng, H.; Zhang, Y.; Yang, H.; Tang, Z.; Tan, L.; Tang, Y.; Wu, L. The investigation into the different Co species over Silicalite-1 via modulating heat-treatment atmosphere for propane dehydrogenation. *Mol. Catal.* **2022**, *530*, 112580. [CrossRef]

33.　Jeon, N.; Oh, J.; Tayal, A.; Jeong, B.; Seo, O.; Kim, S.; Chung, I.; Yun, Y.J. Effects of heat-treatment atmosphere and temperature on cobalt species in Co/Al_2O_3 catalyst for propane dehydrogenation. *J. Catal.* **2021**, *404*, 1007–1016. [CrossRef]

34.　Ge, M.; Chen, X.; Li, Y.; Wang, J.; Xu, Y.; Zhang, L. Perovskite-derived cobalt-based catalyst for catalytic propane dehydrogenation. *React. Kinet. Mech. Catal.* **2020**, *130*, 241–256. [CrossRef]

35. Gao, Y.; Peng, L.; Long, J.; Wu, Y.; Dai, Y.; Yang, Y. Hydrogen pre-reduction determined Co–silica interaction and performance of cobalt catalysts for propane dehydrogenation. *Micropor. Mesopor. Mater.* **2021**, *323*, 111187. [CrossRef]

36. Hu, Z.-P.; Qin, G.; Han, J.; Zhang, W.; Wang, N.; Zheng, Y.; Jiang, Q.; Ji, T.; Yuan, Z.-Y.; Xiao, J.; et al. Atomic Insight into the Local Structure and Microenvironment of Isolated Co-Motifs in MFI Zeolite Frameworks for Propane Dehydrogenation. *J. Am. Chem. Soc.* **2022**, *144*, 12127–12137. [CrossRef]

37. Bulavchenko, O.A.; Cherepanova, S.V.; Malakhov, V.V.; Dovlitova, L.S.; Ishchenko, A.V.; Tsybulya, S.V. In situ XRD study of nanocrystalline cobalt oxide reduction. *Kinet. Catal.* **2009**, *50*, 192–198. [CrossRef]

38. Ji, Y.; Zhao, Z.; Duan, A.; Jiang, G.; Liu, J. Comparative Study on the Formation and Reduction of Bulk and Al$_2$O$_3$-Supported Cobalt Oxides by H$_2$-TPR Technique. *J. Phys. Chem. C* **2009**, *113*, 7186–7199. [CrossRef]

39. Tomic-Tucakovic, B.; Majstorovic, D.; Jelic, D.; Mentus, S. Thermogravimetric study of the kinetics of Co$_3$O$_4$ reduction by hydrogen. *Thermochim. Acta* **2012**, *541*, 15–24. [CrossRef]

40. Chen, C.; Zhang, S.M.; Wang, Z.; Yuan, Z.Y. Ultrasmall Co confined in the silanols of dealuminated beta zeolite: A highly active and selective catalyst for direct dehydrogenation of propane to propylene. *J. Catal.* **2020**, *383*, 77–87. [CrossRef]

41. Li, X.Y.; Wang, P.Z.; Wang, H.R.; Li, C.Y. Effects of the state of Co species in Co/Al$_2$O$_3$ catalysts on the catalytic performance of propane dehydrogenation. *Appl. Surf. Sci.* **2018**, *441*, 688–693. [CrossRef]

42. Wu, Y.; Long, J.; Wei, S.; Gao, Y.; Yang, D.; Dai, Y.; Yang, Y. Non-oxidative propane dehydrogenation over Co/Ti-ZSM-5 catalysts: Ti species-tuned Co state and surface acidity. *Micropor. Mesopor. Mater.* **2022**, *341*, 112115. [CrossRef]

43. Li, Y.; Zhang, Q.; Fu, S.; Kondratenko, V.A.; Otroshchenko, T.; Bartling, S.; Zhang, Y.; Zanina, A.; Wang, Y.; Cui, G.; et al. Active species and fundamentals of their creation in Co-containing catalysts for efficient propane dehydrogenation to propylene. *Chem. Eng. J.* **2023**, *460*, 14177. [CrossRef]

44. Jacobson, D.; Freiser, B. Studies of the Reactions of Group 8 Transition-Metal Ions Fe$^+$, Co$^+$, and Ni$^+$ with Linear Alkanes. Determination of Reaction Mechanisms and MC$_n$H$_{2n}^+$ Ion Structures Using Fourier Transform Mass Spectrometry Collision-Induced Dissociation. *J. Am. Chem. Soc.* **1983**, *105*, 5197–5206. [CrossRef]

45. Freas, R.B.; Campana, J.E. Dehydrogenation of isobutane by oxygen-deficient cobalt/oxygen cluster ions. *J. Am. Chem. Soc.* **1986**, *108*, 4659–4661. [CrossRef]

46. Van Koppen, P.; Brodbelt-Lustig, J.; Bowers, M.; Dearden, D.; Beauchamp, J.; Fisher, E.R.; Armentrout, P. Transition Metal Ion Mediated C–H and C–C Bond Activation of Alkanes: Dynamical Coupling between Entrance and Exit Channel Transition States. *J. Am. Chem. Soc.* **1991**, *113*, 2359–2369. [CrossRef]

47. Van Koppen, P.A.; Bowers, M.T.; Haynes, C.L.; Armentrout, P.B. Reactions of Ground-State Ti$^+$ and V$^+$ with Propane: Factors That Govern C–H and C–C Bond Cleavage Product Branching Ratios. *J. Am. Chem. Soc.* **1998**, *120*, 5704–5712. [CrossRef]

48. Gao, K.; Yoshikai, N. Low-Valent Cobalt Catalysis: New Opportunities for C−H Functionalization. *Acc. Chem. Res.* **2014**, *47*, 1208–1219. [CrossRef]

49. Rodriguez, J.A.; Hanson, J.C.; Frenkel, A.I.; Kim, J.Y.; Perez, M. Experimental and Theoretical Studies on the Reaction of H$_2$ with NiO: Role of O Vacancies and Mechanism for Oxide Reduction. *J. Am. Chem. Soc.* **2002**, *124*, 346–354. [CrossRef]

50. Jeangros, J.; Hansen, T.W.; Wagner, J.B.; Damsgaard, C.D.; Dunin-Borkowski, R.E.; Hebert, C.; Van herle, J.; Hessler-Wyser, A. Reduction of nickel oxide particles by hydrogen studied in an environmental TEM. *J. Mater. Sci.* **2012**, *48*, 2893–2907. [CrossRef]

51. Rasi, N.M.; Ponnurangam, S.; Mahinpey, N. First-principles investigations into the effect of oxygen vacancies on the enhanced reactivity of NiO via Bader charge and density of states analysis. *Catal. Today* **2023**, *407*, 172–181. [CrossRef]

52. Li, Y.; Chen, T.; Zhao, S.; Wu, P.; Chong, Y.; Li, A.; Zhao, Y.; Chen, G.; Jin, X.; Qiu, Y.; et al. Engineering Cobalt Oxide with Coexisting Cobalt Defects and Oxygen Vacancies for Enhanced Catalytic Oxidation of Toluene. *ACS Catal.* **2022**, *12*, 4906–4917. [CrossRef]

53. Kumar, J.; Jung, H.J.; Neiber, R.R.; Soomro, R.A.; Kwon, Y.J.; Hassan, N.U.; Shon, M.; Lee, J.H.; Baek, K.-Y.; Cho, K.Y. Recent advances in oxygen deficient metal oxides: Opportunities as supercapacitor electrodes. *Int. J. Energy Res.* **2022**, *46*, 7055–7081. [CrossRef]

54. Liu, H.; Fu, H.; Liu, Y.; Chen, X.; Yu, K.; Wang, L. Synthesis, characterization and utilization of oxygen vacancy contained metal oxide semiconductors for energy and environmental catalysis. *Chemosphere* **2021**, *272*, 129534. [CrossRef] [PubMed]

55. Zhang, X.; Liu, X.; Zeng, Y.; Tong, Y.; Lu, X. Oxygen Defects in Promoting the Electrochemical Performance of Metal Oxides for Supercapacitors: Recent Advances and Challenges. *Small Methods* **2020**, *4*, 1900823. [CrossRef]

56. Zeeshan, M.; Chang, Q.-Y.; Zhang, J.; Hu, P.; Sui, Z.-J.; Zhou, X.-G.; Chen, D.; Zhu, Y.-A. Effects of Oxygen Vacancy and Pt Doping on the Catalytic Performance of CeO$_2$ in Propane Dehydrogenation: A First-Principles Study. *Chin. J. Chem.* **2021**, *39*, 2391–2402. [CrossRef]

57. Xie, Z.; Yu, T.; Song, W.; Li, J.; Zhao, Z.; Liu, B.; Gao, Z.; Li, D. Highly active nanosized anatase TiO2–x oxide catalysts in situ formed through reduction and Ostwald ripening processes for propane dehydrogenation. *ACS Catal.* **2020**, *10*, 14678–14693. [CrossRef]

58. Li, C.-F.; Guo, X.; Shang, Q.-H.; Yan, X.I.; Ren, C.; Lang, W.-Z.; Guo, Y.-J. Defective TiO$_2$ for propane dehydrogenation. *Ind. Eng. Chem. Res.* **2020**, *59*, 4377–4387. [CrossRef]

59. Zhang, Y.; Zhao, Y.; Otroshchenko, T.; Lund, H.; Pohl, M.-M.; Rodemerck, U.; Linke, D.; Jiao, H.; Jiang, G.; Kondratenko, E.V. Control of coordinatively unsaturated Zr sites in ZrO$_2$ for efficient C–H bond activation. *Nat. Commun.* **2018**, *9*, 3794. [CrossRef]

60. Xie, Z.; Li, Z.; Tang, P.; Song, Y.; Zhao, Z.; Kong, L.; Fan, X.; Xiao, X. The effect of oxygen vacancies on the coordinatively unsaturated Al–O acid-base pairs for propane dehydrogenation. *J. Catal.* **2021**, *397*, 172–182. [CrossRef]

61. Yun, Y.; Araujo, J.R.; Melaet, G.; Baek, J.; Archanjo, B.S.; Oh, M.; Alivisatos, A.P.; Somorjai, G.A. Activation of tungsten oxide for propane dehydrogenation and its high catalytic activity and selectivity. *Catal. Lett.* **2017**, *147*, 622–632. [CrossRef]
62. Golovnya, R.V.; Samusenko, A.L.; Mistryukov, E.A. Analysis of polar compounds on PEG-40M/KF glass capillary columns. *J. High Resolut. Chromatogr.* **1979**, *2*, 609–612. [CrossRef]